ICARUS 97, 211–227 (1992)

Albedo Maps of Pluto and Charon: Initial Mutual Event Results

MARC W. BUIE

Lowell Observatory, 1400 West Mars Hill Road, Flagstaff, Arizona 86001

DAVID J. THOLEN

Institute for Astronomy, 2680 Woodlawn Drive, Honolulu, Hawaii 96822

AND

KEITH HORNE

Space Telescope Science Institute, 3700 San Martin Drive, Baltimore, Maryland 21218

Received November 21, 1991; revised February 18, 1992

We present single-scattering albedo maps of the surfaces of Pluto and Charon based primarily on mutual event observations. The dataset contains 3374 photometric observations that cover 15 different satellite transit events, 14 satellite eclipse events, and other out-of-eclipse photometry spanning 1954 to 1986. The maps consist of a 59 × 29 grid of tiles for each body. We applied the technique of maximum entropy image reconstruction to invert the lightcurves, thus revealing surface maps of single-scattering albedo. The surface of Pluto is seen to have albedo features similar to our previous spot model maps (Buie and Tholen 1989). In particular, a south polar cap is evident in the map of Pluto. The north polar region is brighter than the equatorial regions but is not as bright as the south pole. Single-scattering albedos range from 0.98 in the south polar cap to a low near 0.2 at longitudes corresponding to the lightcurve minimum. The map of Charon is somewhat darker with single-scattering albedos as low as 0.03.

INTRODUCTION

During the past 7 years, many people have worked on the problem of albedo maps for Pluto. The work by Marcialis (1988) and Buie and Tholen (1989) used collections of circular spots on Pluto and a constant albedo on Charon to model the lightcurve of the Pluto–Charon system. One result from Buie and Tholen (1989) was the indication that Pluto has bright polar caps with a dark equatorial belt. Circular spots are adequate when low-resolution data such as rotational lightcurves are modeled. However, this type of model does not have enough flexibility to allow modeling of high time-resolution data from the mutual eclipses between Pluto and Charon.

More recently, Young and Binzel (1990) used large albedo patches on the surface of Pluto to model their satellite transit data without using any rotational lightcurve data. They did not attempt to find a global solution to the albedo distribution, but they modeled the eclipsed hemisphere well enough to point out gross albedo domains. Their model confirms the existence of a south polar cap, but they find no strong evidence for a northern polar cap.

The work presented in this paper is a continuation of the work by Horne *et al.* (1988) and Buie *et al.* (1990) and represents the first attempt to obtain a global solution for the albedo distribution of both Pluto and Charon using rotational lightcurves *and* mutual event data. Unlike other approaches, we use a grid of small tiles on the surface and can adjust each independently to make the model fit the observed data.

DESCRIPTION OF ECLIPSES

Before describing the model, we present a brief description of mutual event phenomena. Rather than classifying an event as a transit, eclipse, or occultation, we use the term "mutual event" to cover all cases where the lightcurve of the system would deviate from the nominal background rotational lightcurve. Throughout this paper, the term "inferior event" will be taken to mean an event where Charon is in front of Pluto at the time of minimum apparent separation. Conversely, "superior events" refer to those events where Charon is behind Pluto.

The occurrence and timing of the mutual events are critically dependent on the orbit of Charon. A series of

0019-1035/92 $5.00

TABLE I
Adopted Orbital and Physical Parameters for Pluto–Charon System

Semimajor axis	19,640	±	320	km
Eccentricity	0.0001	±	0.00010	
Inclination[a]	98.8	±	1.0	deg
Ascending node[a]	222.391	±	0.031	deg
Argument of periapsis[a]	225	±	34	deg
Mean anomaly[b]	259.96	±	0.08	deg
Epoch	JDE 2,446,600.5	=	1986 June 19	
Period	6.387245	±	0.000012	days
Pluto radius	1150	±	7	km
Charon radius	593	±	10	km

[a] Referred to the mean equator and equinox of 1950.0.
[b] Measured from the ascending node.

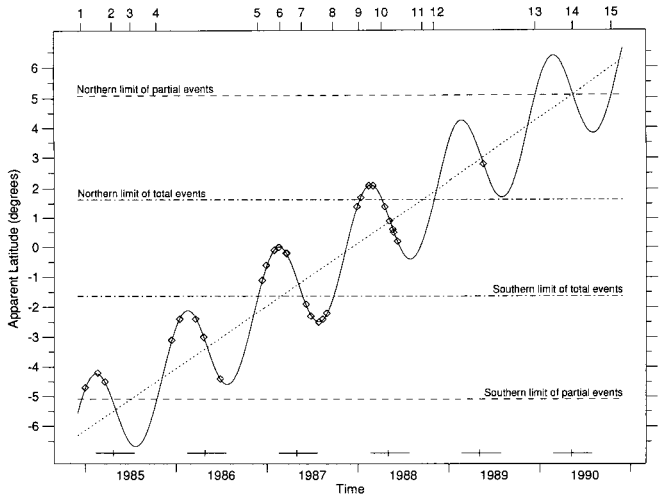

FIG. 1. Geometry and data summary for Pluto–Charon mutual events. This figure contains a plot of the sub-Earth (solid curve) and the subsolar (dotted curve) latitudes on Pluto centered on the season of mutual events. The horizontal lines indicate the boundaries of either partial or total events. Partial events can occur whenever either curve is within the latitude range. Total events can occur when both curves are within the latitude range. Superimposed on the sub-Earth latitude curve are diamond symbols at the times of the event lightcurves modeled in this work. The small bars at the bottom of the figure indicate the nominal observing window for Pluto. The small vertical tick marks indicate opposition and the horizontal bars extend from pre- to postopposition quadrature for each year. The numbers along the top of the plot correspond to the numbers in the first column of Table II which highlights the significant transitions during the complete mutual event season.

papers describes the orbit modeling throughout the mutual event season: Tholen (1985), Tholen *et al.* (1987b and c), and Tholen and Buie (1988, 1992). The modeling work of Tholen *et al.* uses a uniform albedo for Charon and uniform but different albedos for the eclipsed and uneclipsed areas on Pluto for each event. While the uniform albedo assumption is simplistic, timing of the events is the dominant constraint in the modeling of the orientation and period of the orbit.

The orbital parameters adopted for this paper and shown in Table I are from an early orbit solution based on mutual event data through the 1990 apparition. The final orbit solution from Tholen and Buie (1992) differs slightly from the value in Table I but the differences are small and within the stated uncertainties in Table I. As a result, we did not update the orbital parameters and rerun the model fits.

Events occur whenever the subsolar ($\delta_\odot$) or sub-Earth ($\delta_\oplus$) latitude satisfies the relation

$$|\delta| < \text{Arcsin}\left(\frac{r_p \pm r_c}{d}\right), \quad (1)$$

where r_p is the radius of Pluto, r_c is the radius of Charon, and d is the orbital separation. The plus sign holds for the condition of partial overlap and the minus sign holds for the condition of total overlap. For the physical parameters listed in Table I, the critical angle is 5°.09 for partial overlap and is 1°.63 for total overlap at minimum separation.

Figure 1 is a graphical summary of the entire mutual event season. Table II provides an accompanying list of important transitions during the event season. Column 1 contains a number which also appears along the top of Fig. 1. At each of these dates some aspect of the mutual events changes. These dates do not correspond to actual events, merely the time at which $|\delta_\odot|$ and $|\delta_\oplus|$ pass through specific values. The column labeled "overlap" indicates whether there is overlap between the disks of Pluto and Charon. This is equivalent to the condition of $|\delta_\oplus| < 5°.09$. The "shadowing" column indicates when $|\delta_\odot| < 5°.09$, a condition for one body to shadow another. The last two columns indicate whether total events occur. The condi-

TABLE II
Summary of Mutual Event Season

				Total Events	
#	Date	Overlap	Shadowing	Inferior	Superior
1	1984 Dec 16	start	no	no	no
2	1985 Apr 18	stop	no	no	no
3	1985 Jul 03	no	start	no	no
4	1985 Oct 15	start	yes	no	no
5	1986 Nov 27	yes	yes	no	start
6	1987 Feb 27	yes	yes	start	yes
7	1987 May 24	yes	yes	stop	yes
8	1987 Sep 26	yes	yes	start	yes
9	1988 Jan 08	yes	yes	stop	yes
10	1988 Apr 07	yes	yes	start	yes
11	1988 Sep 18	yes	yes	stop	yes
12	1988 Nov 4	yes	yes	no	stop
13	1989 Dec 15	stop	yes	no	no
14	1990 May 12	no	stop	no	no
14	1990 May 14	start	no	no	no
15	1990 Oct 16	stop	no	no	no

tion for totality during inferior events is that both $|\delta_\odot|$ and $|\delta_\oplus|$ be less than 1°.63. For total superior events, either $|\delta_\oplus|$ or $|\delta_\odot|$ must be less than 1°.63. Figure 1 also provides a quick indication of the location of the occulted region as a function of time. When the apparent latitude is south of Pluto's equator (negative), the obscured region on Pluto and Charon is to the north. Therefore, as the events progressed, the obscured region moved slowly from extreme northern latitudes at the start to extreme southern latitudes at the end.

There are a few notable times contained within Table II. The mutual events began between transitions #1 and #2 coincident with the first successful event observations (Binzel *et al.* 1985). However, transition #3, when shadowing began, went unobserved since the orbit predictions were not yet refined enough to show the presence of events. Finally, there appears to have been a very brief period in 1990 (transition #12) when the events stopped. The actual time span where events stopped is very sensitive to the orbit solution and could change with further improvements to the orbit.

Central, or nearly central, events all lasted about 4.5 hr from first to last contact. A proper measurement of the nearby rotational lightcurve takes about 1 hr. Therefore, an event with complete coverage took nearly 6 hr to observe.

In practice, complete coverage of an event is rare. The observing window within a night must be long enough and must be well centered on the event. Observing near opposition helps satisfy these constraints but limits the possible phase angle coverage. Partial coverage of an event is more likely and just as useful.

Despite the partial coverage, most of the events we observed have some coverage of the adjacent out-of-eclipse lightcurve. The exceptions to this occur at the extreme beginning and ending of each opposition of Pluto. A few events represent a mere 45 min of coverage sometime during the eclipse. These extreme cases were constrained by Pluto-rise (or set) on one end and twilight at the other end.

When $|\delta_\odot|$ and $|\delta_\oplus|$ are small enough, an event occurs every 3.2 days (one half of the orbital period). Thus, no single observatory can observe every event even with perfect weather. On average, one event in five will be well placed in the sky for total coverage from a given site. This situation implies that a good event for a single site comes along every 16 days. In 16 days, Charon has revolved two and a half times. Therefore, the good events spaced 16 days apart will alternate between an inferior event and a superior event. Usually a portion of the event 3.2 days earlier or 3.2 days later than the optimally placed event can also be observed. Also note that the 32 day interval between good events of the same type is just slightly longer than the lunar synodic period, which means that consecutive opportunities to observe events near transit either benefited or suffered from similar sky background conditions. As a result, we also emphasized observations away from opposition, despite the shorter window of observability and the resulting partial event coverage, to improve the signal-to-noise ratio of events seen only during bright Moon conditions near opposition.

OBSERVATIONS AND REDUCTIONS

The mutual event data used in this paper were obtained on Mauna Kea with the University of Hawaii 2.24-m and #1 0.61-m telescopes with a single-channel, dry-ice cooled, RCA C31034A (GaAs) photomultiplier equipped with photon counting electronics known as the "Tinsley photometer." Table III summarizes all the observations contained within our present dataset. All mutual event observations used in this model were taken in blue light and transformed to Johnson B magnitudes. All observations were made differentially with respect to a local comparison star. The Johnson magnitudes for these stars were, in turn, determined differentially with respect to SAO 120107, which we have defined to have $B = 9.8966$, $V = 9.2400$, and $(B - V) = 0.6566$. The columns in Table III contain the following information:

Col. 1—UT date of the observations.
Col. 2—Universal Time of the first Pluto observation.
Col. 3—Universal Time of the last Pluto observation.

TABLE III
Summary of Mutual Event Photometry

Event Date (UT)	First Point	Last Point	Event Coverage	N	$\bar{\sigma}$	Observer(s)	Telescope	Std Star
1984 Dec 31	13:51	15:38	O	75	5.3	DJT	UH 2.24-m	85P
1985 Feb 20	10:37	15:16	O1 m 4	186	4.4	DJT	UH 2.24-m	85P
1985 Mar 21	08:05	11:37	4O	135	4.8	DJT	UH 2.24-m	85P
1985 Dec 14	14:42	15:31	4o	25	6.7	DJT	UH 2.24-m	86P
1986 Jan 15	12:28	15:36	4O	105	5.5	DJT	UH 2.24-m	86P
1986 Mar 20	08:11	14:51	m 4O	123	7.4	DJT	UH 2.24-m	86P
1986 Apr 21	06:11	10:54	m 4O	140	7.8	DJT	UH 2.24-m	86P
1986 Jun 27	06:41	11:27	O1 m 4O	140	5.2	DJT	UH 2.24-m	85P
1986 Dec 13	14:43	15:45	m	30	7.7	DJT	UH 2.24-m	87P
1986 Dec 29	13:36	15:18	m3	54	5.3	DJT	UH 2.24-m	87P
1987 Jan 30	11:34	15:19	2m34O	100	4.6	DJT	UH 2.24-m	87P
1987 Feb 18	11:51	15:54	O12	76	7.2	DJT	UH 2.24-m	87P
1987 Mar 19	09:03	13:07	2m34O	159	12.1	MWB	UH 2.24-m	87P
1987 Mar 22	10:11	14:53	O12m	77	4.1	DJT, MWB	UH 2.24-m	87P
1987 Jun 7	07:21	12:34	4O	73	5.3	DJT	UH 2.24-m	86P
1987 Jun 26	07:50	11:56	o12m3	130	4.0	DJT	UH 2.24-m	86P
1987 Jul 28	06:17	09:52	o12m3	102	4.1	DJT	UH 2.24-m	86P
1987 Aug 13	06:10	08:37	m	75	8.9	DJT	UH 2.24-m	86P
1987 Aug 29	05:57	07:54	2m3	64	5.4	DJT	UH 2.24-m	86P
1987 Dec 28	13:58	15:52	2m	50	4.8	DJT	UH 2.24-m	88P
1988 Jan 13	13:05	15:35	m	80	7.3	DJT	UH 2.24-m	88P
1988 Feb 14	11:18	15:52	m 4O	58	13.1	DJT	UH 0.61-m	88P
1988 Mar 1	09:57	15:46	o12m34O	160	6.0	DJT	UH 2.24-m	88P
1988 Apr 18	07:08	14:43	O12m34O	161	3.9	DJT	UH 2.24-m	88P
1988 May 7	06:29	14:49	O12m3	131	6.1	DJT	UH 2.24-m	87P
1988 May 20	06:04	13:05	12m34O	160	4.1	DJT	UH 2.24-m	87P
1988 May 23	10:09	14:26	O12m3	90	3.9	DJT	UH 2.24-m	87P
1988 Jun 8	06:36	13:17	O12m3	117	4.9	DJT	UH 2.24-m	87P
1989 May 19	07:20	13:32	o1 m 4O	180	8.3	DJT	UH 2.24-m	89P

Col. 4—Set of flags indicating what portions of the event were seen. "O" and "o" refer to the out-of-eclipse lightcurve coverage before first contact and after fourth contact. If the amount of out-of-eclipse coverage was greater than 30 min then an "O" is listed. If the amount of coverage was less than 30 min, then an "o" is listed. The notation 1, 2, 3, and 4 indicates which contact was observed. Likewise, an "m" indicates that the midtime of the eclipse was observed.

Col. 5—Total number of photometric observations.

Col. 6—Average uncertainty per point in units of 10^{-3} mag.

Col. 7—Initials of which author collected the data.

Col. 8—The telescope that was used for the observations.

Col. 9—Which comparison star was used for the observations. All stars are from our network of comparison stars as listed in our annual circumstances papers (cf., Tholen and Buie 1988). 85P stands for 1985 Primary, 86P stands for 1986 Primary, and so on.

Table IV provides more details on the circumstances for each of the observed events. The columns contain the following information:

Col. 1—UT date of the event.

Col. 2—Universal Time of first contact (beginning of event).

Col. 3—Universal Time of second contact (beginning of totality).

Col. 4—Universal Time of minimum separation between Pluto and Charon.

Col. 5—Universal Time of third contact (end of totality).

Col. 6—Universal Time of fourth contact (end of event).

Col. 7—Latitude (in degrees) of the sub-Earth point on Pluto during event.

Col. 8—Latitude (in degrees) of the subsolar point on Pluto during event.

Col. 9—Maximum areal obstruction at the deepest point in the event relative to the combined projected area of Pluto and Charon.

Col. 10—Type of event, Charon at inferior (Inf) or superior (Sup) conjunction.

TABLE IV
Circumstances of Observed Mutual Events

Event Date	Ingress		Min	Egress		$\delta_\oplus$	$\delta_\odot$	Max	Event
(UT)	(1)	(2)	Sep	(3)	(4)			Cvrg	Type
1984 Dec 31	10:49	—	11:36	—	12:25	−4.7	−6.1	1%	Sup
1985 Feb 20	12:45	—	13:57	—	15:10	−4.2	−5.8	3%	Sup
1985 Mar 21	06:54	—	07:53	—	08:54	−4.5	−5.7	2%	Inf
1985 Dec 14	11:55	—	13:38	—	15:22	−3.1	−4.2	11%	Inf
1986 Jan 15	10:05	—	12:00	—	13:56	−2.4	−4.0	17%	Inf
1986 Mar 20	07:08	—	09:03	—	10:59	−2.4	−3.6	17%	Inf
1986 Apr 21	05:54	—	07:41	—	09:27	−3.0	−3.4	12%	Inf
1986 Jun 27	07:18	—	09:30	—	10:48	−4.4	−3.0	10%	Sup
1986 Dec 13	12:43	—	14:50	—	17:14	−1.1	−2.1	28%	Inf
1986 Dec 29	11:51	13:23	14:00	14:38	16:26	−0.6	−2.0	21%	Sup
1987 Jan 30	10:14	11:43	12:24	13:06	14:49	−0.1	−1.8	21%	Sup
1987 Feb 18	14:08	15:37	16:18	17:00	18:38	+0.0	−1.7	21%	Sup
1987 Mar 19	08:03	10:03	10:13	10:33	12:23	−0.2	−1.5	31%	Inf
1987 Mar 22	12:42	14:12	14:52	15:33	17:03	−0.2	−1.5	21%	Sup
1987 Jun 7	04:13	05:50	06:45	06:52	08:46	−1.9	−1.1	21%	Sup
1987 Jun 26	08:05	09:40	10:40	10:47	12:37	−2.3	−0.9	21%	Sup
1987 Jul 28	06:34	08:07	09:06	09:19	11:00	−2.5	−0.8	21%	Sup
1987 Aug 13	05:48	—	08:17	—	10:12	−2.4	−0.7	31%	Inf
1987 Aug 29	05:02	06:34	07:26	07:51	09:24	−2.2	−0.6	21%	Sup
1987 Dec 28	13:07	14:49	15:12	16:18	17:47	+1.4	+0.1	21%	Sup
1988 Jan 13	12:20	—	14:23	—	16:58	+1.7	+0.2	34%	Inf
1988 Feb 14	10:51	—	12:49	—	15:18	+2.1	+0.4	32%	Inf
1988 Mar 1	10:07	11:39	12:05	12:58	14:29	+2.1	+0.5	21%	Sup
1988 Apr 18	07:43	09:39	09:59	10:21	12:06	+1.4	+0.8	26%	Inf
1988 May 7	11:35	13:25	13:58	14:18	16:07	+0.9	+0.9	26%	Inf
1988 May 20	06:09	07:59	08:37	08:51	10:47	+0.6	+0.9	27%	Inf
1988 May 23	10:48	12:23	13:16	13:55	15:26	+0.5	+1.0	21%	Sup
1988 Jun 8	10:02	11:53	12:33	12:41	14:44	+0.2	+1.1	31%	Inf
1989 May 19	07:44	—	09:46	—	11:35	+2.8	+3.0	15%	Inf

All times and dates are reported in a geocentric frame. No lighttime corrections have been applied.

The out-of-eclipse data used to constrain the rotational lightcurve of the system are the same dataset modeled in Buie and Tholen (1989). These data cover 1954 to 1986 with 11 distinct lightcurves. The earliest data were taken when the sub-Earth latitude on Pluto was 55°S. Since then, the sub-Earth point has been moving northward and has crossed the equator. Over this time, the lightcurve amplitude has increased from 0.12 to 0.3 mag and the mean brightness has decreased by 0.2 mag. We attempt to fit this behavior simultaneously with the mutual event data. For a complete discussion of the rotational lightcurve dataset, consult Buie and Tholen (1989).

The complete dataset modeled in this paper contains 1679 inferior event measurements (15 different events), 1377 superior event measurements (14 different events), and 318 out-of-eclipse measurements spanning the time range of 1954 to 1986. The grand total is 3374 data points.

More data exist that were taken at other observing sites such as Cerro Tololo, La Palma, McDonald, Palomar, Kitt Peak, other telescopes around Tucson, and other assorted sites. We obtained some of these data, but most of them were taken by other observers and are not yet readily accessible. We have not yet used any of our own data from other sites for two reasons. The first reason is that we do not want to worry about working across different instrumental photometric systems at this early stage of analysis. The second reason is that most of the other data were taken at Johnson V wavelengths. There are many reports of spectral differences between Pluto and Charon: Tholen *et al.* (1987a), Fink and DiSanti (1988), Sawyer *et al.* (1987), and Binzel (1988). Before beginning a two-color albedo model for Pluto and Charon, we first want to complete a single-color albedo map. Once all the data are drawn together, the definitive dataset may be as

much as three to four times larger (although there will be duplicate coverage on some events).

The typical time resolution of our data from the UH 2.24-m telescope is 1 to 2 min per point. The time resolution and signal-to-noise ratio are somewhat worse for the data from the UH #1 0.61-m telescope. The deepest inferior events are about 0.5 mag. Superior events are systematically shallower with a maximum depth of 0.17 mag. The best nights yielded data with average uncertainties of 0.004 mag per point. Most nights had uncertainties less than 0.010 mag.

Our standard method of data reduction includes corrections for time variable extinction within a night. On most nights the extinction varied by small but measurable amounts (no more than 10% variation from the mean for the night). We were able to remove the effects of these variations because of our frequent comparison star measurements (every 15 to 20 min).

We have not yet adopted final standard star magnitudes for 1985 Primary, 1986 Primary, etc. We are still using the published magnitudes found in the series of circumstances papers (e.g., Tholen and Buie 1988). Therefore, there may still be small systematic errors between events measured with respect to different stars at the level of 0.003 mag. The quality of the calibration is not good enough for the final albedo analysis but it is sufficient to allow us to begin developing initial maps.

Before fitting a model to the data, we transformed the photometry to a Johnson B magnitude at the mean opposition distance (39.5 AU heliocentric, 38.5 geocentric). We did not correct the photometry to a constant phase angle. The computation of a model magnitude includes the effect of the actual phase angle for each observation.

MODEL

The model for Pluto and Charon consists of two spheres whose surfaces are broken up into spherical-rectangular pixels, called tiles. Each surface is divided into a grid with 59 tiles in the direction of longitude and 29 tiles in the direction of latitude. This array size corresponds to ~6° angular resolution on both surfaces. At the equator, 6° corresponds to a spatial resolution of about 120 × 120 km on Pluto and 60 × 60 km on Charon. Mutual event data provide direct constraints on half of the 3422 tiles in the model. Out-of-eclipse lightcurve data provide the sole constraint on the other half of the tiles.

The sizes for Pluto and Charon, the orbital parameters for Charon, and the orbit for the barycenter taken from the appropriate year of the *Astronomical Almanac* define the observing geometry for each measurement. The orbital and physical parameters in Table I are identical to the values we were using at the time the 1990 circumstances were initially computed (Tholen and Buie 1992). Since that time, the orbit has been improved somewhat. However, we did not feel the changes were large enough to be important for this work.

The longitude system for the surface of Pluto is essentially unchanged from our spot model work. We continue to use the definition of north for Pluto based on the angular momentum vector and we are also using an east longitude scale to maintain a right-handed coordinate system. We have made a slight modification to the 0° longitude reference point on Pluto. Allowing for the possibility of a nonzero eccentricity of Charon, we now define the 0° meridian to pass through the sub-Charon point when Charon is at periapse. The definition for Charon's longitude system is similar. The 0° longitude on Charon passes through the sub-Pluto point when Charon is at periapse. The longitude system chosen for Charon is similar to systems used for other satellites where 0° longitude is seen at superior conjunction. With this longitude system, the eclipsed hemispheres of both objects span the hemisphere from $-90°$ to $+90°$ east longitude. The actual span of eclipsed longitudes is somewhat less due to the rotation of Pluto during an eclipse.

There remains the possibility that correlations between albedo and our orbit solution exist. For now we are treating the orbit solution and albedo maps as separable quantities. We also assume that the atmosphere of Pluto is perfectly transparent, an assumption that may need reexamination if the absorbing haze layer interpretation of the stellar occultation lightcurve by Elliot *et al.* (1989) proves to be correct.

The amount of sunlight reflected from Pluto and Charon is computed using the simplest form of the Hapke scattering theory as defined in Hapke (1981). This theory has been improved on since 1981 (Hapke 1984, 1986) but the amount of information available on the Pluto–Charon system is not complete enough to determine all the new parameters implicit in the more recent formalism.

Our model allows for an arbitrary viewing and illumination direction and can fully account for rotation during eclipses. To compute a model magnitude we integrate the bidirectional reflectance (Eq. 16 from Hapke 1981) over the visible and illuminated surface. For the backscatter function, $B(g)$, we use Hapke's empirical functions, Eqs. 13 and 14. There are three unknown parameters for each tile: the single-scattering albedo w, the single particle phase function $P(g)$ (where g is the phase angle), and the mean particle spacing h. Note that the quantity, h, used here is for use in the old backscatter function and is not the same quantity as derived in Hapke (1986).

We did not feel it was necessary to use a function for $P(g)$ because the range of phase angles is small for Pluto (0°.5 to 1°.9 in our dataset). Instead, we used a constant value. Furthermore, we did not allow $P(g)$ and h to vary from tile to tile, preferring instead to use a global value.

The single-scattering albedo is the only quantity allowed to vary across the surface. Each tile in the grid is thus characterized by its single-scattering albedo.

The values for P and h were chosen to be consistent with the observed global properties of the Pluto–Charon system. Given a phase coefficient of 0.037 mag/° (Buie and Tholen 1989) and a mean single-scattering albedo, there is a family of values of P and h that will reproduce the phase coefficient for a uniform sphere. For this work, we chose the approximate values of $h = 0.3$ and $P = 3.0$ which correspond to a phase coefficient of 0.034 mag/degree for $w = 0.8$ over the entire surface. These values were chosen from the set for these constraints by picking a pair that gave a geometric albedo in the range expected for Pluto. This treatment is only an approximation since the phase effect will depend on w, which varies across the surface. Without disk-resolved data over a wider range of phase angles, it is difficult to do better. The values chosen for P and h are not substantially different from similar values derived for other satellites observed by the Voyager spacecrafts. In particular, McEwen *et al.* (1988) derived $h = 0.15$ and $P = 2.3$ for Io (similar phase angles and wavelength). This comparison is not meant to imply that the surfaces of Pluto and Io are similar. The comparison indicates that the values we used are at least plausible. Not enough attention has yet been given to these quantities to provide a useful conclusion about microscopic surface properties.

One advantage of using the Hapke bidirectional reflectance function is that the theory includes the effect of limb-darkening. There is no need for an albedo and a separate nonphysical limb-darkening coefficient for which there are no independent constraints. Another advantage of our application of the Hapke theory is the ability to compute the effects of a nonzero phase angle rather than needing to model these effects.

Because of the large angular size of each tile, the numerical integration over the visible surface was very inaccurate during mutual events. To provide a smoother integration as a function of time during an event, we split each tile into a 3 × 3 grid. A sub-tile was included in the numerical integral if it was neither eclipsed nor in shadow. This technique was useful in conserving computer time, while being sufficient to reduce the numerical integration errors below the level of the random noise in the data.

MAXIMUM ENTROPY IMAGE RECONSTRUCTION

The general problem of inverting eclipse lightcurves has been discussed for many years in the study of binary stars. Some of these same techniques have been adapted for use in modeling lightcurves of Pluto. Two recent examples are the spot models of Marcialis (1988) and Buie and Tholen (1989). One serious problem with these spot models is that a solution based on minimizing χ^2 is not unique. Indeed, Buie and Tholen (1989) presented two models that fit the out-of-eclipse lightcurves equally well. This problem of nonuniqueness worsens as the number of free parameters in the model increases.

Our approach to fitting a map to the lightcurve data now employs the method of maximum entropy image reconstruction. This method has been used in a variety of fields including astronomy (see Gull and Daniell 1978 for an early example). Skilling and Gull (1985) present a good survey of this technique with examples based on the software we used.

The maximum entropy (ME) approach fits a model to a set of data by applying two basic constraints. The first is a data constraint imposed by using the familiar statistic,

$$\chi^2 = \frac{1}{M}\sum_{k=1}^{M}\left(\frac{d_k - f_k}{\sigma_k}\right)^2, \tag{2}$$

where d_k and f_k are the observed and predicted data, and σ_k is the measured or estimated uncertainty of d_k. The data constraint requires $\chi^2 = C_{\text{aim}}$ for the resultant model image, where C_{aim} is the goodness-of-fit to the data desired in the model solution.

The second constraint applied in the construction of the model image is the maximum entropy constraint. In this context, the entropy of the image is given by

$$S = \sum_{j=1}^{N} I_j - D_j - I_j \cdot \ln\left(\frac{I_j}{D_j}\right), \tag{3}$$

where I_j is the image value at tile j, D_j is the corresponding default value, and N is the number of tiles in the entire model image (Pluto and Charon combined).

When combined—maximize S subject to $\chi^2 = C_{\text{aim}}$—the ME method will return a unique image. This image represents an optimal balance between entropy and the data. Where the data strongly constrain the image, the entropy constraint has little influence on the reconstruction. Entropy constrains the image more where fewer data constraints exist (i.e., the uneclipsed hemispheres of Pluto and Charon). This behavior is especially useful in this application since the amount of evidence constraining each tile varies dramatically over the surface.

In an ideal case where the data *and* their uncertainties are perfectly known and the model is a perfect representation of the system being measured, C_{aim} and thus the final χ^2 will be unity. Unfortunately, in the real world there are often unmeasured systematic or random errors, bad measurements, or imperfect models. The entropy constraint will do nothing to improve or worsen the fit to the data. Instead, it allows the choice of a unique solution from the set of solutions where $\chi^2 = C_{\text{aim}}$. A solution with

$\chi^2 < 1$ may indicate uncertainties that are too large. On the other hand, $\chi^2 > 1$ indicates an imperfect fit to the data which could be caused either by uncertainties that are too small or by an incomplete model.

The default image mentioned in Eq. (3), D, is crucial to the ME reconstruction since it controls the entropy function. Differentiating Eq. (3) with respect to I_j will show that the entropy function takes on a maximum value of 0 when the value of each image pixel is equal to the corresponding value from the default image. When the entropy is maximized subject to $\chi^2 = C_{\text{aim}}$, those pixels strongly constrained by the data move well away from their default values, while poorly constrained pixels remain close to their default values. In this way the ME image results from a competition or balance between the "pull of the data," exerted through the χ^2 constraint, and the "pull of the entropy" toward the default image.

The general practice in ME image reconstruction is to define the default values in terms of weighted geometric averages over the image values:

$$\log D_k = \sum_{j=1}^{N} W_{kj} \cdot \log I_j \Big/ \sum_{j=1}^{N} W_{kj}. \tag{4}$$

The simplest and probably the most commonly used form is the uniform default image obtained by setting $W_{kj} = 1$, so that all pixels have a default value equal to the geometric mean over the entire image. With this uniform default image, the ME image is the answer to the specific question: What is the "most nearly uniform" positive image that fits the data?

A drawback of using the uniform default image is that the entropy pulls image values back toward the default level, leading to a bias in which local maxima are underestimated and local minima are overestimated. The bias can be relatively strong in the case of uniform defaults, because the extreme values are well away from the default level. This bias is discussed by Bryan and Skilling (1980) in the context of an image deconvolution problem, but it is a general feature of ME and many other reconstruction algorithms. In tomography applications, such as those applied to our Pluto mapping problem, the bias can cause nonlocal artifacts (see for example the discussion of Horne 1985).

Bryan and Skilling (1980) propose the use of a statistic different from χ^2 to reduce the bias by strengthening the pull of the data. We follow Horne (1985) in choosing a nonuniform default image in order to reduce the pull of the entropy. Specifically, we use the weights W_{kj} in Eq. 4 to make the default values for each pixel be an average of that pixel and its eight nearest neighbor pixels rather than an average of the entire image. Thus the default image is a smoothed or blurred version of the current image. In this case the entropy becomes insensitive to the large-scale structure of the image. We may refer to this default as a "curvature" default, because the entropy becomes a measure of the local image curvature rather than of departures from its global mean value. With curvature defaults, the ME solution will deliver the "smoothest" positive image that fits the data. The tendency to bias extreme values is diminished because the image values are much closer to their defaults.

As seen in Eq. (3), I must stay in the range $(0,\infty)$. However, the model image sought was the single-scattering albedo of the surface, which lies in the range $[0,1]$. To match the two ranges, we mapped I over the semiinfinite range onto w by using the function

$$w_j = 1 - \exp(-I_j). \tag{5}$$

This function also protects against w taking on the exact values of 0 and 1 which correspond to particles that are perfectly absorbing and perfectly transparent, respectively. We also tried $w_j = I_j/(1 + I_j)$, but the reconstruction did not converge. Therefore, applying the ME reconstruction maximizes S by direct manipulation of the model image, I, with the default image, D. The expression in Eq. (5) transforms I into the single-scattering albedo map upon which the model fluxes depend.

We accomplished the ME reconstruction by using the 1985 version of MEMSYS, a subroutine package written and distributed by Maximum Entropy Data Consultants, Ltd. Skilling and Bryan (1984) provide a description of the general algorithm behind this software. Burch *et al.* (1983) describe details of the FORTRAN implementation we used.

The algorithm proceeds from an initially uniform image and iteratively adjusts the image. At each iteration, the default image is computed from the previous iteration on the image. The final result is an image that maximizes S for $\chi^2 = C_{\text{aim}}$. The method provides an additional statistic,

$$T = 1 - \frac{\nabla S \cdot \nabla \chi^2}{|\nabla S||\nabla \chi^2|}, \tag{6}$$

that vanishes when the entropy gradient (∇S) is parallel to the χ^2 gradient ($\nabla \chi^2$). For a converged solution, $\chi^2 = C_{\text{aim}}$ and $T \ll 1$. In linear problems, this technique is not only powerful, but fast as well. Each new step toward the final image depends on quadratic models of S and χ^2 which assume that the predicted data are linear in I. Thus, rapid convergence (usually in about 30 iterations) depends on linearity. Our lightcurve inversion problem is decidedly nonlinear due to the Hapke bidirectional reflectance function and the mapping of I onto w. This difficulty does not affect the final map, only how many iterations one needs to compute to get the map.

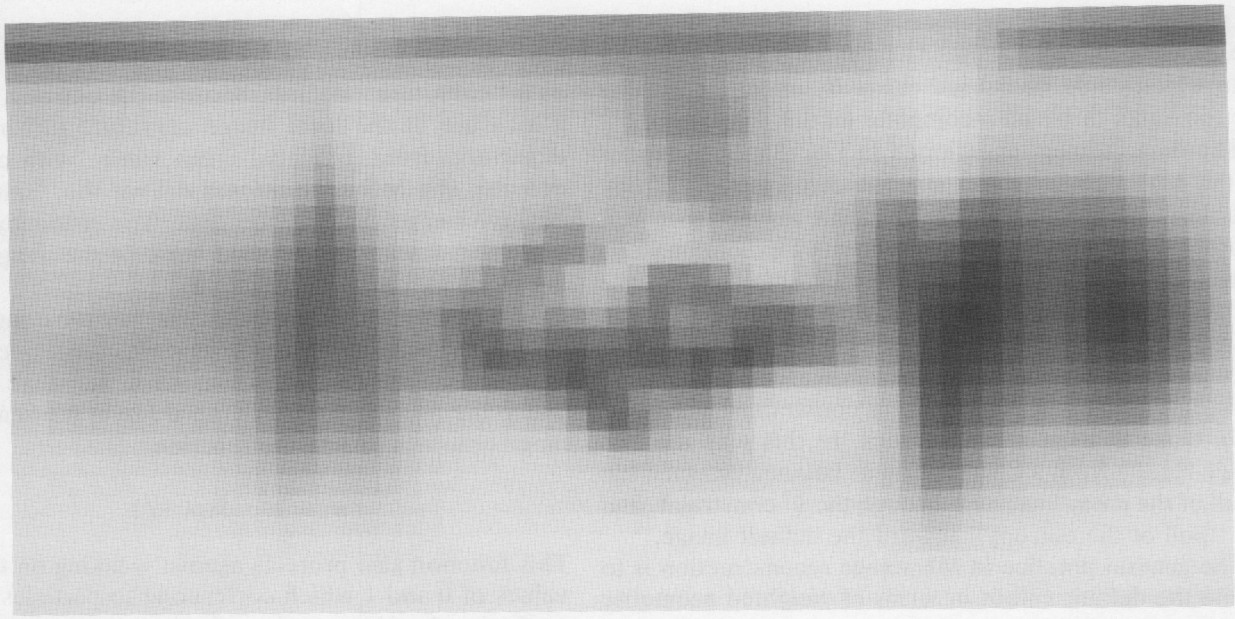

FIG. 2. Single-scattering albedo map of Pluto. This map is shown with the same latitude and longitude scale as the contour plot below.

RESULTS

The starting point for this reconstruction was a uniform map. After 1300 iterations with MEMSYS, we obtained our final maps of the single-scattering albedo for Pluto and Charon. These maps are shown in Figs. 2–5 both as images and as contour plots. The final fit from these maps has a reduced χ^2 of 4.7 which is good but not perfect (i.e., $\chi^2 = 1$). This solution almost reached final convergence but with the final value of $T = 0.2$, the solution is not perfect. It is impossible to quantify what effect the lack of perfect convergence has on the final map. In general,

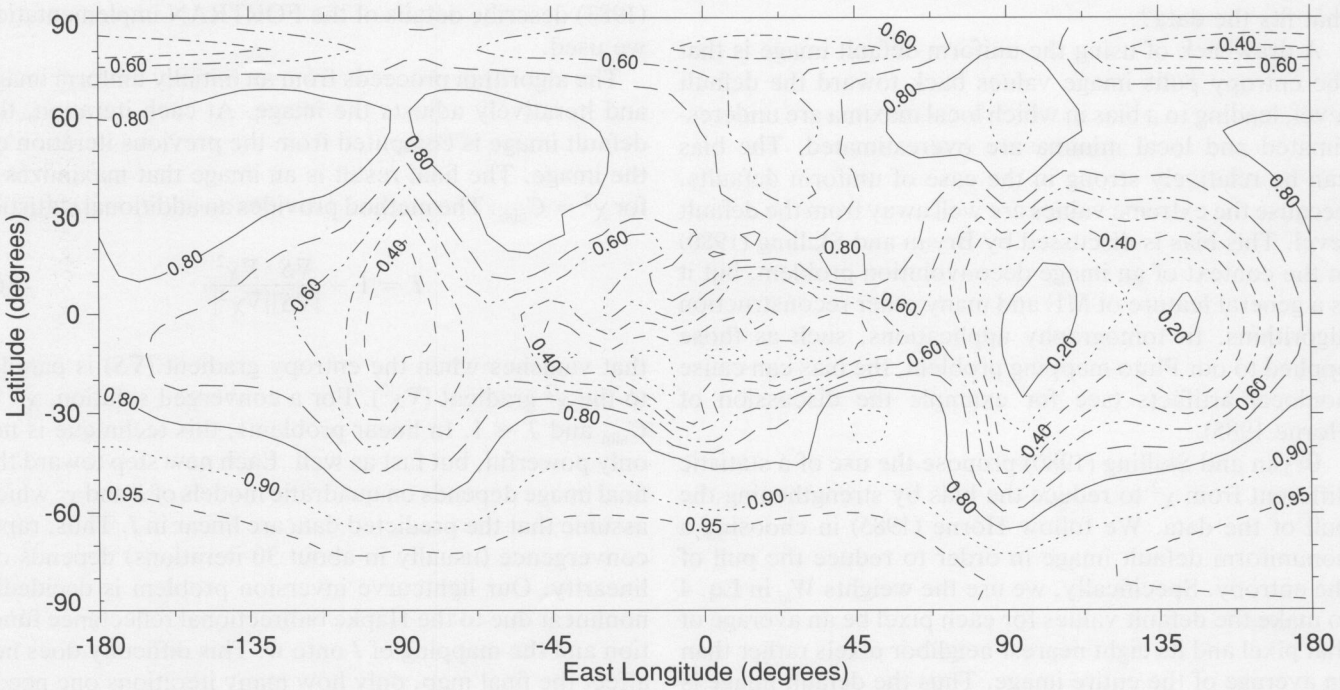

FIG. 3. Contour plot of the single-scattering albedo of Pluto.

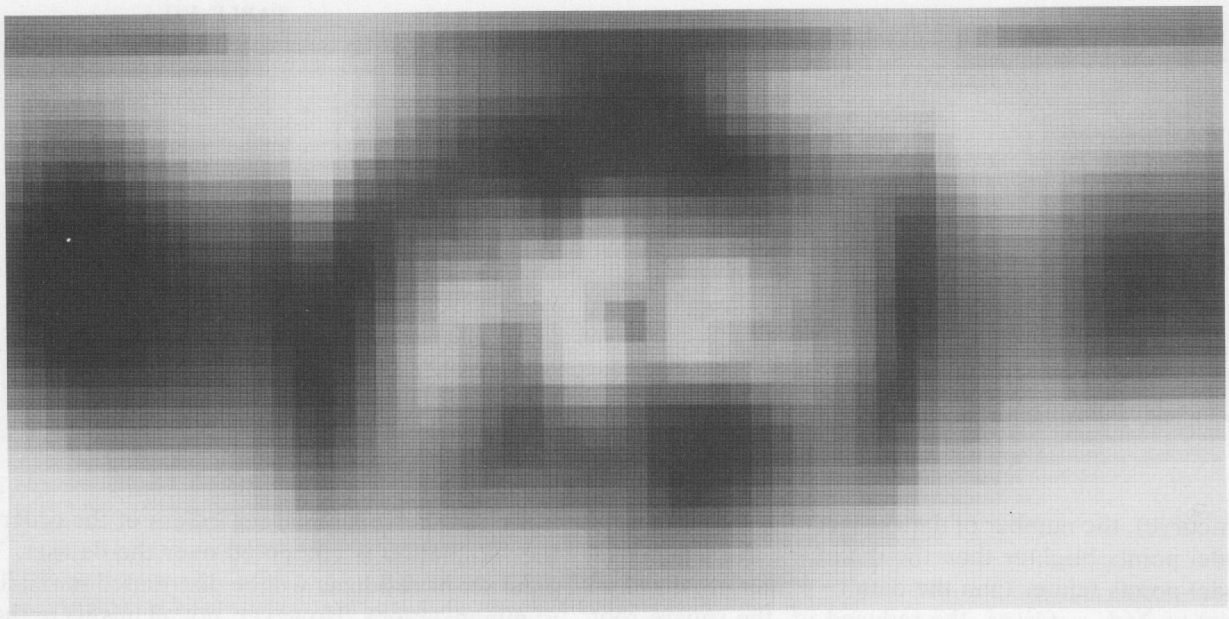

FIG. 4. Single-scattering albedo map of Charon. This map is shown with the same latitude and longitude scale as the contour plot below.

$T \neq 0$ indicates that the value of entropy for the given χ^2 is not at its maximum. A lower value for entropy indicates more fine structure in the map than can be supported by the data. The broad albedo domains should be reliable, but structure on the scale of a few tiles may be spurious.

Table V contains a summary of the residuals from the out-of-eclipse photometry previously fit with our spot model (Buie and Tholen 1989). Tables VI and VII contain a summary of the superior and inferior events, respectively, for each mutual event in our dataset (listed in Table III). Each of these tables lists the following quantities from left to right: the date (or year) of the event (or rotational

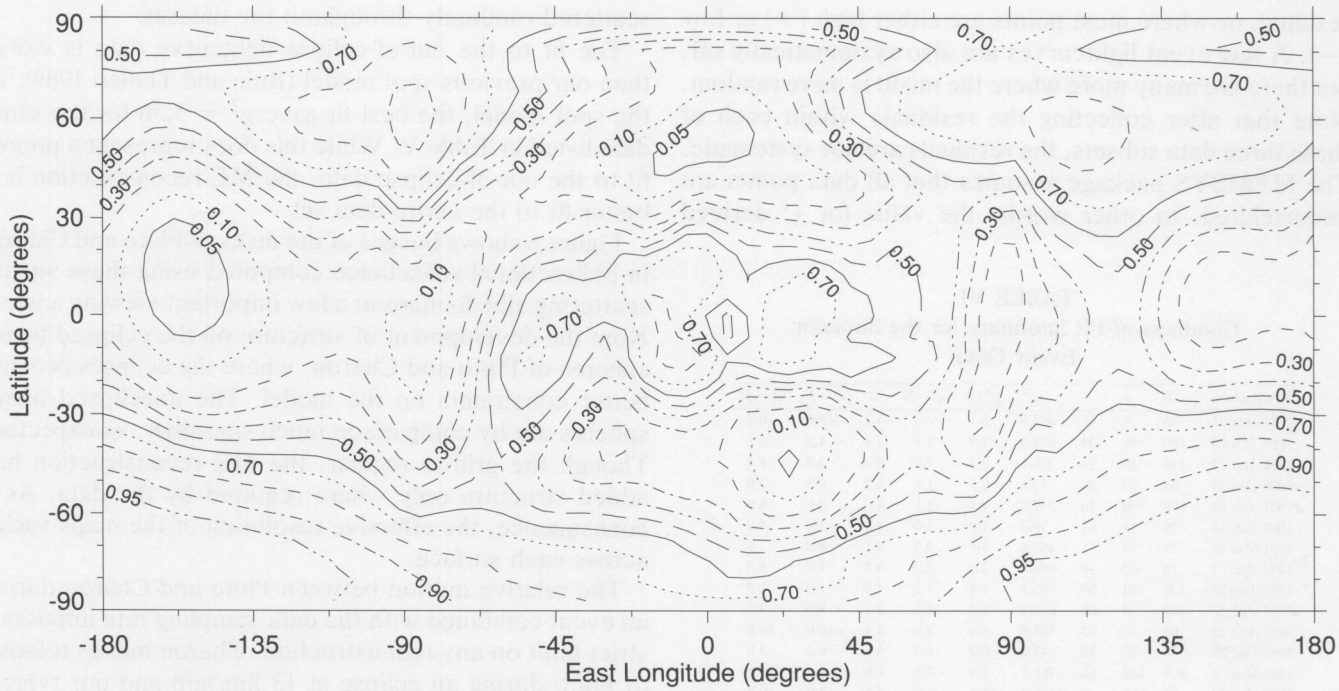

FIG. 5. Contour plot of the single-scattering albedo of Charon.

TABLE V
Goodness-of-Fit Summary for the Rotational Lightcurve Data

Data Set	N	+	−	χ^2	χ^2/N	$\chi/\sqrt{N}$	$\bar{\sigma}$	$\overline{d-f}$	$\overline{\lvert d-f\rvert}$
1954 Apparition	6	2	4	21.3	3.6	1.9	5.8	− 2.2	6.9
1955 Apparition	15	2	13	105.0	7.0	2.6	7.0	−12.2	12.6
1964 Apparition	14	2	12	359.2	25.7	5.1	9.7	−33.2	33.8
1971 Apparition	1	1	0	4.2	4.2	2.0	30.0	61.4	61.4
1972 Apparition	14	8	6	41.4	3.0	1.7	22.5	9.8	28.9
1973 Apparition	3	1	2	3.4	1.1	1.1	30.0	−18.7	19.3
1975 Apparition	12	4	8	11.7	1.0	1.0	48.4	−13.7	33.4
1980 Apparition	26	26	0	1098.4	42.2	6.5	5.2	24.4	24.4
1981 Apparition	35	32	3	888.7	25.4	5.0	4.1	13.5	13.8
1982 Apparition	44	25	19	891.8	20.3	4.5	6.4	5.5	16.8
1983 Apparition	77	50	27	628.0	8.2	2.9	6.6	2.7	10.2
1984 Apparition	27	13	14	109.4	4.1	2.0	10.0	− 3.0	15.2
1986 Apparition	44	2	42	2365.2	53.8	7.3	4.7	−18.8	20.1
Total	318	168	150	6527.6	20.5	4.5			

TABLE VII
Goodness-of-Fit Summary for the Inferior Event Data

Event Date	N	+	−	χ^2	χ^2/N	$\chi/\sqrt{N}$	$\bar{\sigma}$	$\overline{d-f}$	$\overline{\lvert d-f\rvert}$
1985 Mar 21	135	70	65	328.3	2.4	1.6	4.8	0.2	5.9
1985 Dec 14	25	8	17	36.0	1.4	1.2	6.7	− 4.2	6.6
1986 Jan 15	105	17	88	519.8	5.0	2.2	5.5	− 8.3	9.8
1986 Mar 20	123	60	63	199.9	1.6	1.3	7.4	− 0.4	7.0
1986 Apr 21	140	35	104	262.5	1.9	1.4	7.8	− 5.7	9.0
1986 Dec 13	30	14	16	42.1	1.4	1.2	7.7	0.1	7.8
1987 Mar 19	159	97	62	219.4	1.4	1.2	12.1	4.0	11.9
1987 Aug 13	75	50	25	100.3	1.3	1.2	8.9	4.6	8.3
1988 Jan 13	80	12	68	283.1	3.5	1.9	7.3	−10.3	12.1
1988 Feb 14	58	6	52	146.5	2.5	1.6	13.1	−16.6	17.6
1988 Apr 18	161	120	41	422.7	2.6	1.6	3.9	3.2	4.8
1988 May 7	131	38	92	174.3	1.3	1.2	6.1	− 3.2	5.5
1988 May 20	160	94	65	250.3	1.6	1.3	4.1	1.5	4.0
1988 Jun 8	117	75	41	281.6	2.4	1.6	4.9	2.3	6.1
1989 May 19	180	147	33	665.2	3.7	1.9	8.3	10.8	12.8
Total	1679	843	836	3931.8	2.3	1.5			

lightcurve), the number of data points (N), the number of model points brighter than the data (+), the number of model points fainter than the data (−), unnormalized χ^2 equal to $\Sigma(d_i - f_i)^2/\sigma_i^2$, the reduced χ^2, the square root of the reduced χ^2 indicating how many standard deviations the model fit is away from the data, the average error bar ($\bar{\sigma}$), the average residual ($\overline{d-f}$), and the scatter in the fit ($\overline{|d-f|}$). The last three columns are in units of 10^{-3} mag.

A careful examination of the error summaries reveals a few interesting points. The rotational lightcurve data, representing 9% of the dataset, accounts for 41% of the total χ^2. In general, the out-of-eclipse data are not fit nearly as well as the eclipse data where the misfit is usually a systematic offset from the model. All such cases can be readily seen where the scatter is the same as the average residual, or where most points are either high (+) or low (−). A few event lightcurves are also systematically off, but there are many more where the misfit is more random. Note that after collecting the residuals within each of these three data subsets, the residuals are not systematic. The MEMSYS package assumes that all data points are uncorrelated. In other words, the value for χ^2 derived from Eq. (2) is identical regardless of the order in which the summation is computed over the dataset. The complete set of residuals will be distributed normally in most χ^2 minimizations. However, not all misfits to the data are the same. For example, it is possible to have a model fit where within an event the residual was constant and that constant was different for each event. Another model could have the same total error distribution, but have the errors randomly distributed across the entire data-set so no single event has a statistically significant systematic misfit. These two cases are indistinguishable for our choice of data constraint, χ^2, but we consider a systematic misfit unacceptable. A consecutive sequence of data points that are 2σ low should be more significant than the same number of data points with the same residuals scattered randomly throughout the dataset.

TABLE VI
Goodness-of-Fit Summary for the Superior Event Data

Event Date	N	+	−	χ^2	χ^2/N	$\chi/\sqrt{N}$	$\bar{\sigma}$	$\overline{d-f}$	$\overline{\lvert d-f\rvert}$
1984 Dec 31	75	4	71	385.5	5.1	2.3	5.3	−10.0	10.3
1985 Feb 20	186	50	134	543.3	2.9	1.7	4.4	− 4.2	6.1
1986 Jun 27	140	40	99	355.1	2.5	1.6	5.2	− 3.9	6.4
1986 Dec 29	54	29	24	49.5	0.9	1.0	5.3	0.5	3.9
1987 Jan 30	100	30	70	437.9	4.4	2.1	4.6	− 3.9	8.4
1987 Feb 18	76	14	61	76.0	1.0	1.0	7.2	− 4.0	5.7
1987 Mar 22	77	75	1	469.6	6.1	2.5	4.1	8.8	.8
1987 Jun 7	73	63	10	283.4	3.9	2.0	5.3	7.8	8.9
1987 Jun 26	130	91	39	185.5	1.4	1.2	4.0	1.9	3.9
1987 Jul 28	102	4	98	656.8	6.4	2.5	4.1	− 9.0	9.2
1987 Aug 29	64	2	62	435.6	6.8	2.6	5.4	−12.6	12.6
1987 Dec 28	50	25	25	47.0	0.9	1.0	4.8	− 0.2	3.9
1988 Mar 1	160	103	55	361.4	2.3	1.5	6.0	3.4	6.9
1988 May 23	90	90	0	1105.6	12.3	3.5	3.9	12.9	12.9
Total	1377	620	757	5392.1	3.9	2.0			

The fit to the out-of-eclipse lightcurve data is worse than our previous spot model (Buie and Tholen 1989). In the spot model, the best fit gave $\chi^2 = 5.56$ for the same data listed in Table V. While this does represent a poorer fit to the out-of-eclipse data, the ME reconstruction is a better fit to the entire data set.

Figure 6 shows images of the disks of Pluto and Charon in bidirectional reflectance computed using these single-scattering albedo maps at a few important viewing angles. Note the development of structure on the eclipsed hemispheres of Pluto and Charon, where the eclipses provide better constraints on the model. The uneclipsed hemispheres are by comparison much smoother, as expected. Though the grid is regular, the ME reconstruction has added structure only where required by the data. As a consequence, the effective resolution of the maps varies across each surface.

The relative motion between Pluto and Charon during an event combined with the data-sampling rate imposes a strict limit on any reconstruction. Charon moves relative to Pluto during an eclipse at 13 km/min and our typical lightcurve time resolution is about 1 min. Therefore, we

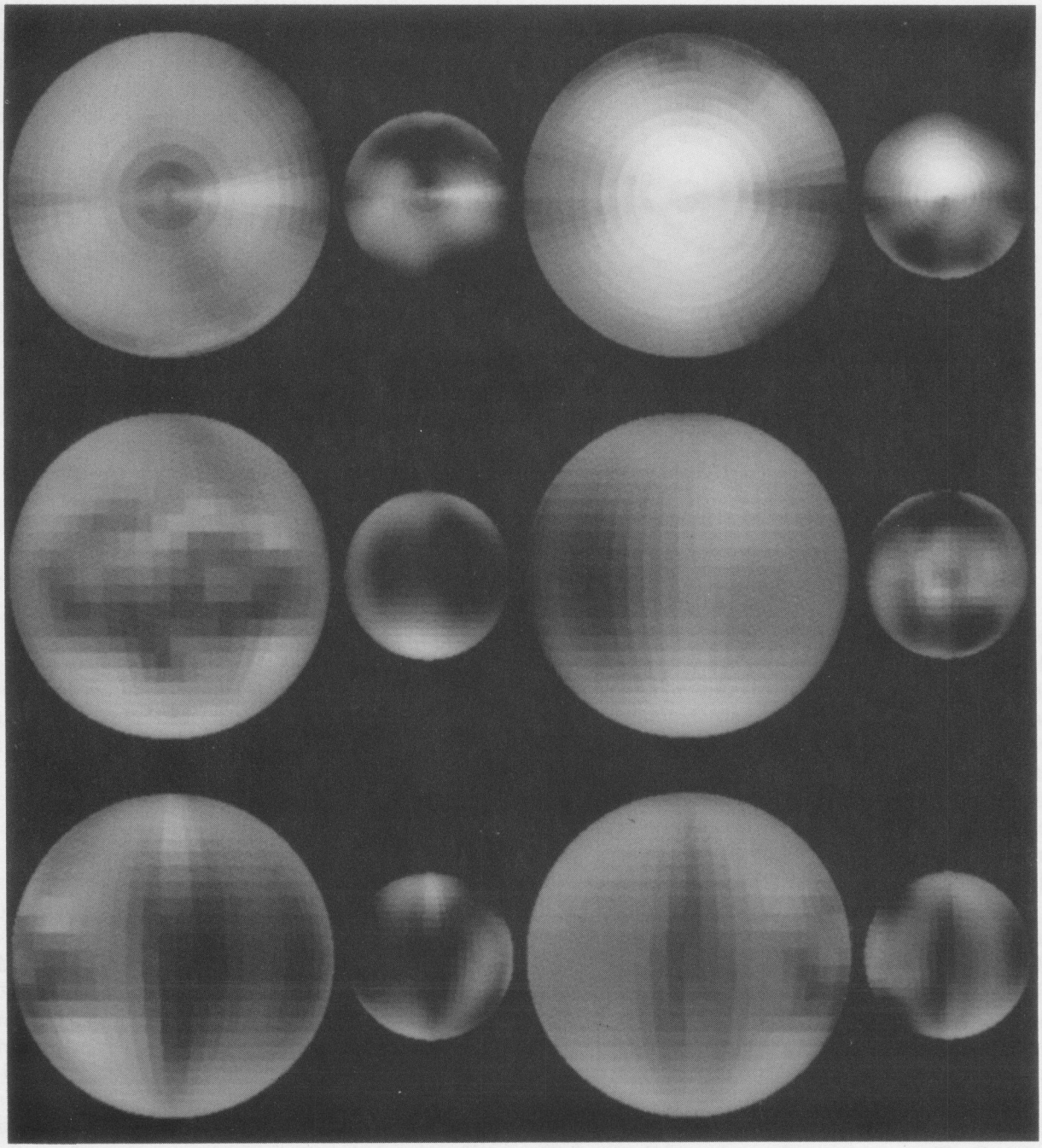

FIG. 6. Bidirectional reflectance images of Pluto and Charon. These images are renderings of Pluto and Charon using the maps in Figs. 2 and 4. The reflectance of each point on the surface is computed using the Hapke equations. The top two images show the system from directly above the north pole (left) and the south pole (right). The middle two images show the equatorial views of the system at a sub-Earth longitude of 0° (left) and 180° (right). Pluto's eclipsed hemisphere is at 0° and Charon's eclipsed hemisphere is at 180°. The bottom pair shows equatorial views at 90° and 270° east longitude. Pluto and Charon's north pole are toward the top in the equatorial views.

expect a "perfect" reconstruction might be as good as 13 km but not better. However, the resolution of our maps is still far from this limit.

The overall appearance of the maps confirms our previous spot model results in showing the polar regions to be brighter than the mean. In particular, the southern pole is very bright and looks very much like a polar cap. The north pole is not nearly as bright and is difficult to characterize as a polar cap. The northern midlatitudes are still brighter than the equatorial regions, but we see a decrease

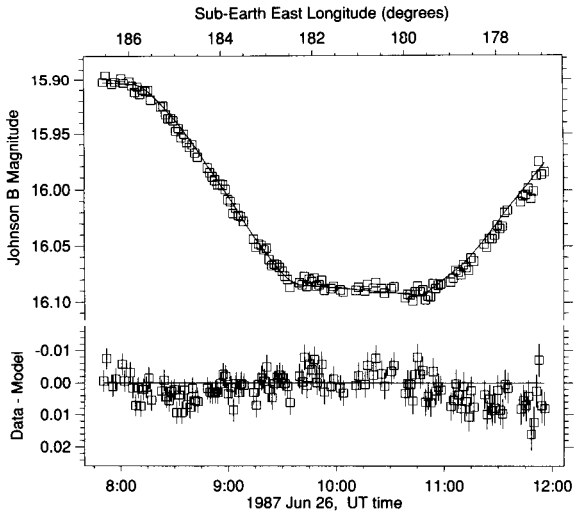

FIG. 7. Data and model fit from a total superior event. The top plot is the data from a total occultation of Charon by Pluto and Pluto's shadow (squares) plotted with the model calculations (solid curve). The bottom plot shows the residuals from the fit.

in albedo near the north pole. In our spot model, there is a north polar cap of radius 59° which was located 10° off the pole at longitude 196°. The maps shown in Figs. 2 and 3 show some similarity. The southern boundary of the $w = 0.8$ contour extends further to the south at a similar longitude as the location of the spot model cap and the secondary bright spot. While the location match is good, our new map has a lower single-scattering albedo. The spot model needed $w = 0.999$ to fit the data, a value considerably brighter than the albedo in our maps. As in the spot model, there is a large dark albedo patch responsible for the rotational lightcurve minimum which is readily apparent near the equator and 100° east longitude. The spot model located its dark spot ($w = 0.4$) at a latitude of $-1.9°$ and a longitude of 110°. Given the simplistic nature of our spot model and the much more limited data set, the correspondence with our new maps is very good.

The range of single-scattering albedos in the maps is very large. On Pluto, w ranges from about 0.2 up to 0.98, while on Charon the map ranges from 0.03 to 0.98. The apparent larger contrast on Charon is not significant since the half-cap artifact (discussed below) controls the high albedo limit. Overall, Charon is darker, consistent with our previous global albedo results (e.g., Tholen and Buie 1988).

Despite the quality of the maps, there are several features in the maps that are not real. The most striking are the north–south bands located at 90° and 270° east longitude. These longitudes represent the limb of each body at the time of the mutual events. Since most of the data come from events, these tiles are almost always seen on the limb. These bands could be explained if the limb darkening provided by the Hapke model is too weak. If so, the model would compensate by making the limb tiles darker to simulate the additional limb darkening. The artifacts may also be caused by the coarse tiles and represent an error in the numerical integration for the model calculation. Errors in the orbit determination and sizes of the bodies could also cause limb artifacts. The most likely source for these artifacts is in our numerical model and is discussed in the next section.

There is also a rather severe artifact on the south pole of Charon. The image of Charon in the far upper right of Fig. 6 shows a sharp horizontal line across the disk which corresponds to the south limb during an event. Superior event data constrain the dark half of the pole while out-of-eclipse photometry provides the sole constraint on the bright half. Of the two halves, the darker portion should be more accurate. Wherever there are no data to the contrary, our ME reconstruction will make the albedo on Charon the same as on Pluto. While it is *possible* to have half of a polar cap, our experience with planetary and satellite surfaces so far tells us this is apparently nonphysical.

We can remove the polar artifact on Charon in one of two ways. The first is to collect separate lightcurves of Pluto and Charon. These data will allow a separation of the combined light and will prevent raising the albedo of Charon on the uneclipsed hemisphere to match that of Pluto. The second approach is to change the model to discourage this apparently nonphysical result. One method involves using a different default image. Recall that the default image for this model has a variable resolution depending on the latitude leading to much less longitudinal smoothing at the poles than on the equator. It would be much more reasonable for poorly constrained polar material to have similar albedos to other tiles at the poles than it would be for the uneclipsed tiles to be similar to Pluto. Constructing the default image by smoothing on a uniform spatial scale would help discourage fine structure at the poles unless the data required such structure.

The model fit to the data is very good, despite the artifacts and the relatively large value of χ^2. Some of the best fit lightcurves and their corresponding model calculations are shown in Figs. 7 and 8. Shown in Fig. 7 is a lightcurve from a total eclipse of Charon. The fit to the data is almost perfect but a small amount of systematic misfit is present in the residuals, particularly on egress.

The two lightcurves shown in Fig. 8 are from two transits of Charon across Pluto. The time between the two events is just one month and yet the lightcurves are substantially different. In particular, there is structure in the lightcurves between second and third contact caused by albedo patterns on the surface. In the 1988 April 18

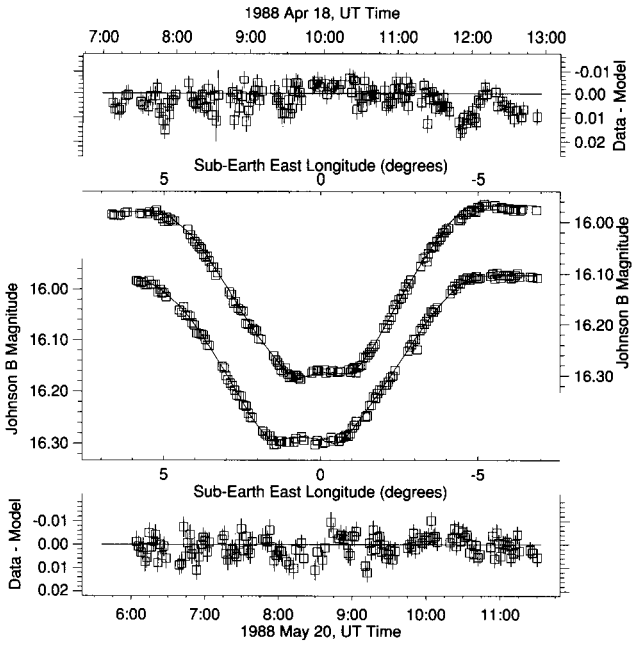

FIG. 8. Data and model fit from two inferior events. The top two curves are from the 1988 April 18 transit of Charon across Pluto. Shown are the residuals (top) and the data where the individual points represent the data and the solid curve represents the model. The bottom two curves are from the 1988 May 20 transit. Again, the data are shown against the model and the residuals are plotted at the bottom. All four curves are plotted against the same sub-Earth longitude axis. The apparent shift in the eclipse is due to the changing aspect between Charon and its shadow.

lightcurve, the brightness increases just after second contact. This increase is not seen in the 1988 May 20 event. Figure 9 illustrates the difference in geometry between the two events and which map features affect the lightcurves. Note that the northern limit of the occulted region of Pluto is almost exactly the same for the two events. Charon and its shadow have exchanged places at the northern eclipse boundary. On the other hand, obscuration from the 1988 April 18 event extends much farther to the south. There is a slight break in the slope of the ingress portion of the lightcurve just before second contact as the darker equatorial zone begins to be uncovered. As second contact approaches, Charon continues to obscure bright polar material. The minimum occurs as the bright polar material begins to be uncovered. Once past second contact the lightcurve is flat because of the relatively flat longitudinal brightness structure. In this case, latitudinal albedo variations cause the fine-scale lightcurve structure.

SIMULATED RECONSTRUCTION

Just how good are the reconstructed maps of Pluto and Charon? Ideally, one would like to have a quantitative measure of the resolution as a function of latitude and longitude as well as of uncertainties on the fitted albedo values. The resolution is only weakly related to the grid of tiles on the surface. A map can never have a higher resolution than the grid, but with this technique it can always have a lower resolution than the grid. The amount of information in the map and thus the resolution achieved depends on the amount of information in the data. Locations that are well constrained by data will be reconstructed with higher resolution than a region that is poorly constrained. The uneclipsed hemispheres of both Pluto and Charon will be reconstructed with a very low spatial resolution because there is no evidence in the data for fine structure. The best resolution is achieved on portions of the eclipse hemispheres that are sampled with many different events. In this case, the constraints are very strong and the information contained in the map will be much greater. However, fine sampling and a large number of data contraints do not imply fine structure in the reconstruction. The map could be very smooth even with ample constraints simply because the surface is indeed uniform.

Unfortunately, no known method provides a quantitative determination of the information content (i.e., resolution or photometric accuracy) in a reconstructed map. We can provide some feeling for the accuracy of these maps with a simulated reconstruction from a dataset with a known model. By looking at the reconstruction compared to the original map, we can get some feeling for what is possible with a reconstruction in this particular case. Our fake data were computed by integrating over the fake Pluto and Charon while replicating the observing geometry and noise from the real dataset. From this simulated noisy dataset, we reconstructed a map from the fake data for comparison with the original fake image.

Figure 10 shows the results of the simulation. The fake map has a background level of $w = 0.1$ from 0 to 180° east longitude and $w = 0.2$ on the other half of the surface. Superimposed on this background is an array of conical spots whose peak brightness is $w = 0.99$ in the center. There are also two spots at each of the poles. The fit to the fake data provided by the reconstructed map is very good, with $\chi^2 = 1.1$ after 700 iterations. This solution was not allowed to proceed to final convergence due to a limitation of computer time. The simulations took nearly 5 hr of CPU time on a Cray 2 supercomputer. For comparison, the Pluto–Charon reconstructions consumed about 10 CPU hr and nearly 1300 iterations.

This test case was designed to show the regions on the surfaces where our dataset can provide high spatial resolution information on Pluto and Charon. As expected, the reconstruction works best on the eclipsed hemispheres. Also, this simulation points out that the data provide much better constraints on the southern polar regions than on the northern polar regions on the eclipsed hemisphere. This example shows a characteristic prop-

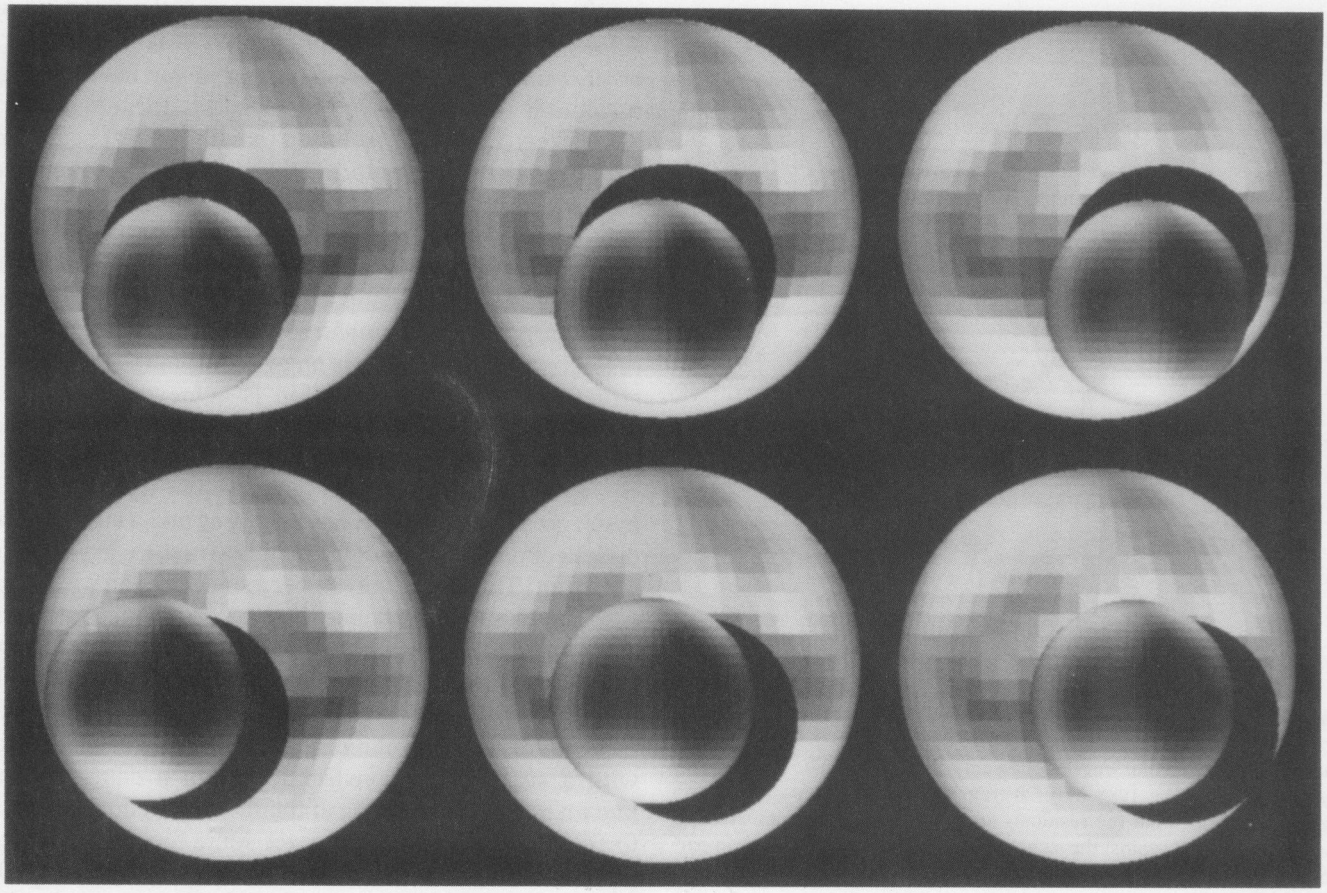

FIG. 9. Images during transits plotted in Fig. 8. From left to right, the top three images correspond to the geometry on 1988 April 18 at 09:40, 09:56, and 10:20 UT. These times correspond to second contact, minimum separation, and third contact. The bottom three images are from 1988 May 20 at 7:58, 8:31, and 8:51 UT. Pluto's and Charon's north poles are toward the top in all images.

erty of a maximum entropy reconstruction. The poorly constrained regions appear to be much smoother than well constrained areas. Note that the artifacts at longitudes 90 and 270° are present even in this test. These results give us confidence that similar artifacts in the Pluto–Charon reconstructions have nothing to do with true albedo structure on the surface of Pluto or Charon. Furthermore, these artifacts are not caused by an incorrect orbit, incorrect sizes for the bodies, nonspherical shape, unmodeled atmospheric hazes, or incorrect limb darkening in our model, since these are all, by definition, correct for the simulated data. The artifacts may be a consequence of the granularity of the numerical integration but our efforts to date are inconclusive.

The simulated reconstruction used the same grid in the output map as was used in the original map on which the fake data was based. This simulation cannot be used to infer the ultimate resolution possible with our dataset. We have shown that portions of the surface are reconstructed at a scale commensurate with the size of the tiles. To test high spatial resolution features against our dataset, we would need to run simulations with much smaller pixels on both the input map and the reconstruction grid. Eventually this will be an important test to run but it was beyond the scope of this initial work.

DISCUSSION

The maps presented in this work are but a sample of what will be possible with the complete dataset. So far, our modeling efforts have not revealed conclusive evidence for temporal variability of the surface albedo. Despite the many free parameters in the model, ME reconstruction will not provide a satisfactory solution if the model omits essential physics. A likely failure of the model would be an inability to fit the early rotational lightcurves. This model does yield a relatively poorer fit to *all* the rotational lightcurves. We suspect that this misfit is due to fewer observations and poorer absolute calibration. However, we cannot rule out the possibility that the poorer fit to the preevent data is caused by an overall darkening of the surface from 1954 to the present.

The fit to the data of $\chi^2 = 4.7$ and $T = 0.2$ provided by these maps represents the best reconstruction that

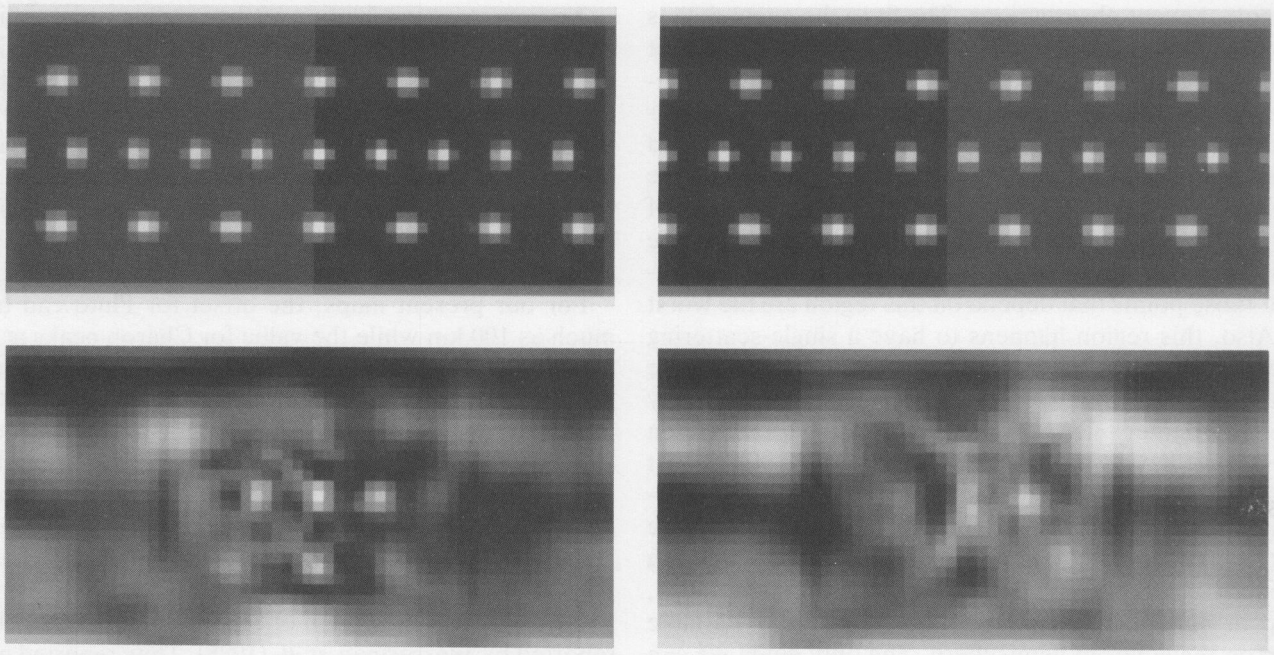

FIG. 10. Original and reconstructed fake maps. The two images on the left are for Pluto, the two on the right are for Charon. The top two images show the original fake images used to create the fake data. The bottom pair shows the results after ME reconstruction. The maps are displayed with exactly the same longitude ranges as in Fig. 2 and Fig. 4 so the eclipsed hemispheres are in the center of the maps. The reconstructed images have been scaled up by a factor of 1.25 and 1.64 for the left and right panels, respectively.

we could achieve with this model. There are several limitations that we found that must contribute to the failure of the model to achieve a χ^2 of unity. We have yet to finalize the calibration of our comparison stars and there may be small systematic errors within the mutual event data depending upon which comparison star was used. These systematic errors will be greatly reduced upon final reduction of the comparison stars. Another obvious limitation is an incomplete physical description of the surfaces of Pluto and Charon. Examples might include time variability of the surface, atmospheric haze effects, and incorrect orbital and physical parameters. There are, however, other algorithmic limitations that we must eliminate before calling the physics of the model into question.

The artifacts in the maps are serious deficiencies in these reconstructions, particularly the half-cap on the south pole of Charon. The reflected flux provided by this artifact is substantial and is very important in the model fit to the earliest rotational lightcurve data. The south pole of Pluto already has an albedo well over 0.95, about as bright as it can be, and so the extra flux required to fit the early lightcurve data is placed on Charon's south pole. Removing this artifact from the map may be difficult to do and still fit the older data.

Of all the physical parameters of the system, the semimajor axis remains the most uncertain and the most important quantity. The mutual event modeling has determined the relative scale of the system quite well. However, the actual single-scattering albedo of the brightest regions will depend critically on the absolute size of the system. If the semimajor axis is larger than measured by Beletic *et al.* (1989) at 19,640 km, the single-scattering albedos in our maps would decrease. Our modeling shows that it will be hard to reconcile a smaller semimajor axis since some areas cannot be made brighter. Such a conclusion is also supported by the Charon occultation results (Walker, 1980). The occultation lower-limit of 600 km for the radius of Charon is consistent with the value in Table I, but the semimajor axis cannot be much smaller and still result in a consistent radius for Charon. Also, the latest analysis of the Pluto stellar occultation in 1988 calls for a larger Pluto and thus a larger semimajor axis (R. Millis, private communication). The interpretation of the Pluto stellar occultation results is uncertain due to a lack of understanding of the atmospheric structure and the possible presence of a substantial haze layer. We anxiously await new and improved measurements of the absolute scale of the system. Having a more precise value will allow us to use the surface albedos to place limits on the age of the volatiles on the surface. For the moment, we must be content with knowing there are very bright regions on the surface.

Aside from the obvious artifacts discussed, how much of the maps is real, or at least well determined? The maps should be quite good in regions of the surface constrained

by mutual event observations. The fit to the event data is very good and we expect the albedo distribution cannot change much without affecting the fit. The nonevent longitudes are less known because there are far fewer observations, and of those observations all are disk-integrated measurements with very low spatial resolution. Of these poorly constrained regions, the southern polar regions of the uneclipsed hemispheres of Pluto and Charon are the most uncertain portion of the maps. Of all the data modeled, those points that depend on this region are the worst fit. Also, this region happens to have a single-scattering albedo very close to unity. If the absolute size of the system is larger than we have assumed, this region may be even brighter relative to the surrounding areas. Given the size we have used, a small absolute scale will distort the map near these very bright areas as surrounding terrain is made brighter in the map to compensate for the lack of freedom in the areas where the single-scattering albedo is already unity. Finally, in evaluating the maps, keep in mind that their resolution is strongly variable even on the eclipsed hemisphere. The only guide we can provide to estimate the spatial resolution as a function of location is furnished in our simulated reconstruction.

Another limitation of the present model is that the size of the tiles at the equator may be too large for modeling the mutual event data. As the number of tiles increases, the fit may improve. The penalty paid for increasing the number of tiles is a substantial increase in the computing time required. The present model resolution was a compromise between the available computing resources and computing an accurate numerical integral over the visible surface. Based on the lightcurve time resolution and the relative speeds of Pluto and Charon during an occultation, mapping portions of the surface should approach 20-km resolution. Such a map would require a 20-fold increase in computing resources assuming the number of iterations required for convergence is independent of resolution (not a good assumption for nonlinear problems).

Several improvements to these maps are in progress. We are changing the tiling pattern to save memory (fewer tiles at the poles). The tiles in the maps of Pluto and Charon should have the same area and not be the same angular size. Resizing the Charon tiles would lead to a further decrease in the number of tiles. We are also changing the method of computing the default image to attempt to remove some of the artifacts in our present maps. Also, the final Mauna Kea dataset will be about 40% larger and provide more uniform coverage over the entire event season.

Other improvements to these maps would come from an accurate measurement of the individual lightcurves of Pluto and Charon. Such lightcurves would help break the ambiguity in the present data and provide separate constraints that would directly prevent such mapping artifacts as the half-cap on Charon.

An important application of these maps is determining an accurate semimajor axis and measuring the individual densities through observations of the barycentric wobble. Any astrometric measurement reports the position of the center-of-light for either the system or for each individual body. To relate these measurements into the positions of the bodies themselves, we must know or model the offset between the center-of-light and the center-of-figure. With these maps, we can compute that offset.

For our present maps, the offset for Pluto can be as much as 100 km while the value for Charon peaks at ~20 km. These calculations are not yet good enough to correct for the effect but do serve to illustrate the size of the offset. In comparison, the semimajor axis reported by Beletic *et al.* (1989) is 19,640 ± 320 km. The effect from our present maps is a factor of three smaller than the present uncertainty, but it is obvious that the center-of-light offset must be included before the absolute scale of the system can be measured more accurately.

A preliminary indication of this effect has already been reported by Wasserman *et al.* (1988). They reported oscillations of the center-of-light for the system relative to the predicted position. They measured the period of this oscillation and got a good match with the orbital period of Charon. Their center-of-light calculations based on our older spot model (uniform Charon) did not match the observations. Their conclusion was that the variegated surface of Charon must also contribute to the center-of-light motion.

Looking to the future, if we are ever successful in sending a spacecraft to Pluto, maps such as these will be invaluable for mission planning. It would be a shame to wait 20 years for a spacecraft flyby only to get back overexposed pictures due to a lack of general knowledge of the surface. Part of the success of the Voyager II flyby of Triton is due to studies of Pluto and recognizing Pluto and Triton as being very similar.

ACKNOWLEDGMENTS

Portions of this work were supported under NASA Grant NGL 12-001-057 (Buie and Tholen), NAGW 1991 (Tholen), and NAGW 1912 (Buie). We also acknowledge computing support from the National Center for Supercomputing Applications at the University of Illinois through a block grant to the Space Telescope Science Institute. MWB is grateful for discussions with J. Skilling during an enlightening train ride in Wyoming. We also thank R. Howell and R. Binzel for inciteful comments.

REFERENCES

BINZEL, R. P. 1988. Hemispherical color differences on Pluto and Charon. *Science* **241**, 1070-1072.

BINZEL, R. P., D. J. THOLEN, E. F. TEDESCO, B. J. BURATTI, AND R. M. NELSON 1985. The detection of eclipses in the Pluto–Charon system. *Science* **228**,1193-1195.

BELETIC, J. W., R. M. GOODY, AND D. J. THOLEN 1989. Orbital elements of Charon from speckle interferometry. *Icarus* **79,** 38–46.

BRYAN, R. K., AND J. SKILLING 1980. Deconvolution by maximum entropy, as illustrated by application to the jet of M87. *Mon. Not. Roy. Astron. Soc.* **191,** 69–79.

BUIE, M. W., AND D. J. THOLEN 1989. The surface albedo distribution of Pluto. *Icarus* **79,** 23–37.

BUIE, M. W., D. J. THOLEN, AND K. HORNE 1990. Albedo map of Pluto and Charon from mutual event observations. *Bull. Am. Astron. Soc.* **22,** 1129.

BURCH, S. F., S. F. GULL, AND J. SKILLING 1983. Image restoration by a powerful maximum entropy method. *Comput. Vis. Graph. Image Process* **23,** 113–128.

ELLIOT, J. L., E. W. DUNHAM, A. S. BOSH, S. M. SLIVAN, L. A. YOUNG, L. H. WASSERMAN, AND R. L. MILLIS 1989. Pluto's Atmosphere. *Icarus* **77,** 148–170.

FINK, U., AND M. A. DISANTI 1988. The separate spectra of Pluto and its satellite Charon. *Astron. J.* **95,** 229–236.

GULL, S. F., AND G. J. DANIELL 1978. Image reconstruction from incomplete and noisy data. *Nature* **272,** 686–690.

HAPKE, B. 1981. Bidirectional reflectance spectroscopy. 1. Theory. *J. Geophys. Res.* **86,** 3039–3054.

HAPKE, B. 1984. Bidirectional reflectance spectroscopy. 3. Correction for macroscopic roughness. *Icarus* **59,** 41–59.

HAPKE, B. 1986. Bidirectional reflectance spectroscopy. 4. The extinction coefficient and the opposition effect. *Icarus* **64,** 264–280.

HORNE, K. 1985. Images of accretion discs–I. The eclipse mapping method. *Mon. Not. Roy. Astron. Soc.* **213,** 129–141.

HORNE, K., M. W. BUIE, AND D. J. THOLEN 1988. Maximum entropy maps of Pluto and Charon from mutual event light curves. *Bull. Am. Astron. Soc.* **20,** 1089.

MARCIALIS, R. L. 1988. A two-spot albedo model for the surface of Pluto. *Astron. J.* **95,** 941–947.

MCEWEN, A. S., T. V. JOHNSON, D. L. MATSON, AND L. A. SODERBLOM 1988. The global distribution, abundance, and stability of SO_2 on Io. *Icarus* **75,** 450–478.

SAWYER, S. R., E. S. BARKER, A. L. COCHRAN, AND W. D. COCHRAN 1987. Spectrophotometry of Pluto–Charon mutual events: Individual spectra of Pluto and Charon. *Science* **238,** 1560–1563.

SKILLING, J., AND R. K. BRYAN 1984. Maximum entropy image reconstruction: General algorithm. *Mon. Not. Roy. Astron. Soc.* **211,** 111–124.

SKILLING, J., AND S. F. GULL 1985. Algorithms and applications. In *Maximum-Entropy and Bayesian Methods in Inverse Problems* (C. R. Smith and W. T. Grandy, Eds.), pp. 83–132. Reidel.

THOLEN, D. J. 1985. Circumstances for Pluto–Charon mutual events in 1986. *Astron. J.* **90,** 2639–2642.

THOLEN, D. J., AND M. W. BUIE 1988. Circumstances for Pluto–Charon mutual events in 1989. *Astron. J.* **96,** 1977–1982.

THOLEN, D. J., AND M. W. BUIE 1992. Circumstances for Pluto–Charon mutual events in 1990 and 1985. In preparation.

THOLEN, D. J., M. W. BUIE, R. P. BINZEL, AND M. L. FRUEH 1987a. Improved orbital and physical parameters for the Pluto–Charon system. *Science* **237,** 512–514.

THOLEN, D. J., M. W. BUIE, AND C. E. SWIFT 1987b. Circumstances for Pluto–Charon mutual events in 1987. *Astron. J.* **93,** 244–247.

THOLEN, D. J., M. W. BUIE, AND C. E. SWIFT 1987c. Circumstances for Pluto–Charon mutual events in 1988. *Astron. J.* **94,** 1681–1685.

WALKER, A. R. 1980. An occultation by Charon. *Mon. Not. Roy. Astron. Soc.* **192,** 47–50.

WASSERMAN, L. H., R. L. MILLIS, O. G. FRANZ, A. R. KLEMOLA, AND C. C. DAHN 1988. Precise astrometry of the Pluto/Charon system. *Bull. Am. Astron. Soc.* **20,** 806.

YOUNG, E. F., AND R. P. BINZEL 1990. A singular value decomposition map of Pluto based on mutual event data. *Bull. Am. Astron. Soc.* **22,** 1128.